

Article

The Fontanamare Discovery (Sardinia Coast, Italy), a Case of Underwater Corrosion of Bronze Coins

Tilde de Caro ^{1,*} , Fiammetta Susanna ², Mauro Francesco La Russa ³ and Andrea Macchia ^{2,3} ¹ CNR ISMN, Strada Provinciale 35d, 9, 00010 Rome, Italy² YOCOCU, Youth in Conservation of Cultural Heritage, Via Torquato Tasso 108, 00185 Rome, Italy; aps@yococu.com (F.S.)³ DIBEST, University of Calabria, Via Pietro Bucci, 87036 Arcavacata, Italy; mlarussa@unical.it

* Correspondence: tilde.decaro@cnr.it

Abstract: This study reports the analytical approach towards nine coins found in wreck A of Fontanamare for understanding the complex corrosion processes that take place in underwater conditions. Optical microscopy (OM) combined with micro-Raman (μ -Raman) spectroscopy, X-ray diffractometry (XRD), and scanning electron microscopy with energy-dispersive X-ray spectroscopy (SEM and EDS) were used to analyze the nature and the microstructure of the corrosion patina in comparison with the non-degraded state of coins. Three main types of corrosion patina based on copper, lead chloride, and carbonate were identified: black, white, and green, and the obtained results demonstrate the complex corrosion processes that take place in underwater conditions. To better understand the role played by different chemical and physical parameters in the corrosion of bronze artefacts in an underwater environment, this study attempts to understand the nature of the patinas on the coins in relation to the specific structural and environmental parameter variation.

Keywords: bronze corrosion; Fontanamare shipwreck; underwater environment



Citation: de Caro, T.; Susanna, F.; La Russa, M.F.; Macchia, A. The Fontanamare Discovery (Sardinia Coast, Italy), a Case of Underwater Corrosion of Bronze Coins. *Minerals* **2023**, *13*, 1085. <https://doi.org/10.3390/min13081085>

Academic Editor: Adrián Durán Benito

Received: 22 June 2023

Revised: 28 July 2023

Accepted: 9 August 2023

Published: 14 August 2023



Copyright: © 2023 by the authors. Licensee MDPI, Basel, Switzerland. This article is an open access article distributed under the terms and conditions of the Creative Commons Attribution (CC BY) license (<https://creativecommons.org/licenses/by/4.0/>).

1. Introduction

Sardinia was the centre of the routes between East and West as early as the 15th century BC, as evidenced by Mycenaean attestations; a strong presence of Cypriot materials followed in the 12th century BC, which testify to exchanges with the Nuragic populations from the point of view of the copper trade and bronze working [1].

The Fontanamare site is located in the Gonnese Bay, on the southwestern side of Sardinia, in the Iglesiente region.

The geomorphological configuration of Fontanamare Bay is characterised by a series of rocks that extend beyond the rocky barrier that runs parallel to the coast between Porto Paglia and Fontanamare. This barrier, combined with the shallow depth of the sea in that stretch, a frontal exposure to the mistral wind, and being almost tangentially to the libeccio wind, has always posed a risk to navigation. Numerous ships that have sunk there have left behind materials that give an indication of this danger.

Wrecks and artefacts of the marine heritage were already known in the 1960s and were the object of numerous depredations.

During underwater campaigns on the southwest coast of Sardinia, in front of Fontanamare (Figure 1A), first in 1965 and then again in 1972, three wreck sites were identified and dated based on the finds of numerous amphorae. Only between 1997 and 1999 did the Superintendence of Cagliari and Oristano conduct some underwater reconnaissance. The research focused on an area south of Sa Punta e S' Arena, extending northeast for one kilometer towards Fontanamare and north-west for about 350 m from the coastline (Figure 1A). The prospecting allowed the identification and survey of eight sites (A–H) (Figure 1B). The wreck sites have been dated mainly based on the pottery contexts: the first site discovered contained Dressel-20-shaped amphorae in its cargo, dated to the first century AD; the

second, dating back to the second century BC, contained Greek–Italian amphorae. These ships were most likely stranded on the cliff following a wrecking event [2,3].



Figure 1. (A) Map of Sardinia showing the location of Fontanamare Bay. (B) Survey of discovery sites marked with an alphabetic letter (A–H). (Image: T. de Caro).

According to the information found in the wrecks, it is feasible to guess the routes the ships took based on the cargo they carried. For example, the wine amphorae and ceramics were likely shipped from southern Italy, whereas the shipment of fish sauce and oil was likely coming from Betica, Spain.

This study is focused on the analytical investigations of nine coins found in shipwreck A of Fontanamare (Sardinia), dated to the third century AD, precisely the Antonine age.

With regard to the numismatic material, an agglomeration of coins of mm 140×115 (weight 2465 gr) called “pane I” (bread) and another of mm 71×55 (weight 91.19 gr), called “pane II” were found in wreck site A, 22 coins with imprints belonging to the pane I, and about 200 loose coins [2,3].

“Pane I” consists of a compact nucleus of coins, where on the external surfaces it is possible to identify about 14 coins. On its external surface, it is possible to observe a texture of a fabric weaving imprint on one side, which suggests that the coins, at the time of the shipwreck, were kept in a canvas sack. It is possible to still see remnants of the original sack’s fibres on a few coins, which serves as confirmation of this (Figure 2).

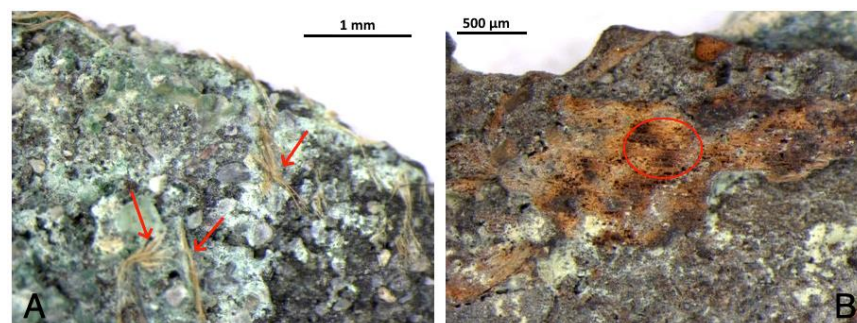


Figure 2. Optical images of coins F14 (A) and F36 (B) that show remnants of the original sack’s fibres (indicated by the red arrows (A) and a highlighted section (B)) of the canvas sack (photos: T. de Caro).

The discovery of the coins thus allowed for the attribution of a certain date to the ship, although only a tiny number are clearly legible. Although the issuing authority cannot be determined with certainty, due to the majority of the coins being either completely unreadable or fractured, it is certain that they are Antoninian coins from the third century AD [3].

The archaeological value of the discovery is high, although in terms of currency, the value of the coins was quite low (about two denarii) and they were probably used for daily payments or sales profits [2].

In this paper, nine bronze coins from the Fontanamare wreck, selected on the basis of the nature of patinas, were investigated for the first time, using a multi-analytical approach combining optical microscopy (OM), micro-Raman (μ -Raman) spectroscopy, and X-ray diffractometry (XRD) to analyze the nature of the patina. Scanning electron microscopy with energy-dispersive X-ray spectroscopy (SEM and EDS) was used to study the microstructure of corrosion products and the nature of alloys by analyzing the surface and cross-section [4].

Studies of the late Roman Empire Antoninian coins discovered in underwater archaeological sites can reveal details about their production. It is also significant for understanding the complex corrosion processes that take place in underwater conditions.

The Marine Environment Corrosion

When a coin is immersed in seawater, its surface interacts with the marine environment, resulting in a very complex corrosive phenomenon, and in a short period, electrochemical mechanisms begin [5–10].

Seawater is the primary corrosive agent in marine corrosion because it is a complex solution of dissolved ionic salts (predominantly sodium (Na^+), chloride (Cl^-), sulphate (SO_4^{2-}), magnesium (Mg^{2+}), calcium (Ca^{2+}), and potassium (K^+)); dissolved gases (O_2 , CO_2); and suspended particulate materials (SPM) that includes mineral particles as well as living and dead plankton, with the addition of biological activity increasing the corrosion rate [11].

Other influencing factors to determine what and how quickly corrosion occurs are seawater temperature [12], the nature of marine currents, pH, and the environmental zone to which the metal is exposed [13].

Typically, as the temperature rises, corrosion progresses more quickly. At the same time, the change in biological activity with temperature is a dominant factor in the sea. The development of marine organisms on the surface of the metal can produce an outer concretion, and behind this concretion, a microenvironment, frequently more protective, can grow. Therefore, because of the increase in temperature, marine organisms grow more quickly and form a protective layer on the metal [12].

Oxygen and carbon dioxide, produced during photosynthetic underwater activities, are the main dissolved gases in seawater. Due to the high concentration of dissolved oxygen, seawater is a strongly oxidizing agent; however, it can turn reducing due to biological activity. This parameter varies depending on the geographical location, as well as the depth and temperature of the water. The corrosion phenomenon becomes more active as the concentration of dissolved oxygen increases. When this parameter falls, for example, at the mud–water interface, the concentration of chloride ions rises. The concentration of dissolved oxygen also affects biological colonization, which takes place on the surface of the metal after a short time of being submerged. Over time, the surface of the metal is covered by biofilm primarily made of aerobic and anaerobic bacteria that might accelerate the corrosion [14,15].

Generally, the marine bacteria strain responsible for microbial corrosion belongs to the sulphate-reducing bacteria group. These bacteria contribute to corrosion by first solubilizing the metal surface with their hydrogenases, then reducing the sulphate to sulphide, causing the dissolution of the metal. The biofilm developed by these bacteria increases with exposure time, and its heterogeneities are also responsible for localized metal surface inhomogeneity, which favors the corrosion process [16].

The depth of the site of finding and the movement of the water is also related to the amount of oxygen in the water and has a pronounced effect on the growth of marine organisms. For this reason, metallic artefacts buried under the seabed have significantly reduced oxygen levels, which can lead to the development of anaerobic conditions around them. Furthermore, sea storms and currents can create movements of the overlying sediments, which change the metal microenvironment from aerobic to anaerobic and vice versa [17].

The average parameters that should be considered for the Sardinian seabed, which is the deposition environment of the coins analyzed, are the following: salinity with an

average value of 35%, with greater values observed in localized places (38.6%), and pH between 7.5 and 8.4 [16].

2. Materials and Methods

2.1. The Antoninianus Coins

The antoninianus coins were introduced under the reign of Caracalla (Marcus Aurelius Antoninus), ca. 214–215 AD [18]. The first coinage contained a percentage of silver, up to 80% of Ag [19].

Then, as a result of the economic crisis due to a severe debasement of the mint, the silver content of the antoninianus gradually declined, hitting its lowest values during the reigns of Gallienus and Aurelianus (270–275 AD), and turned into a bronze coin with a very low silver content (about 2%–3% Ag). Cu and Pb concentrations subsequently rose after Ag content declined [20,21].

The argentiferous bronze coins were produced until the beginning of the reign of Diocletian, when he reintroduced high-quality silver coinage in 294 AD.

In order to better correlate and understand the corrosion processes in submarine conditions related to the microchemical and microstructural properties of the material buried, nine antoninianus coins (Figure 3 and Table 1) from the Fontanamare wreckage have been selected based on the different patina chemical and morphological features.

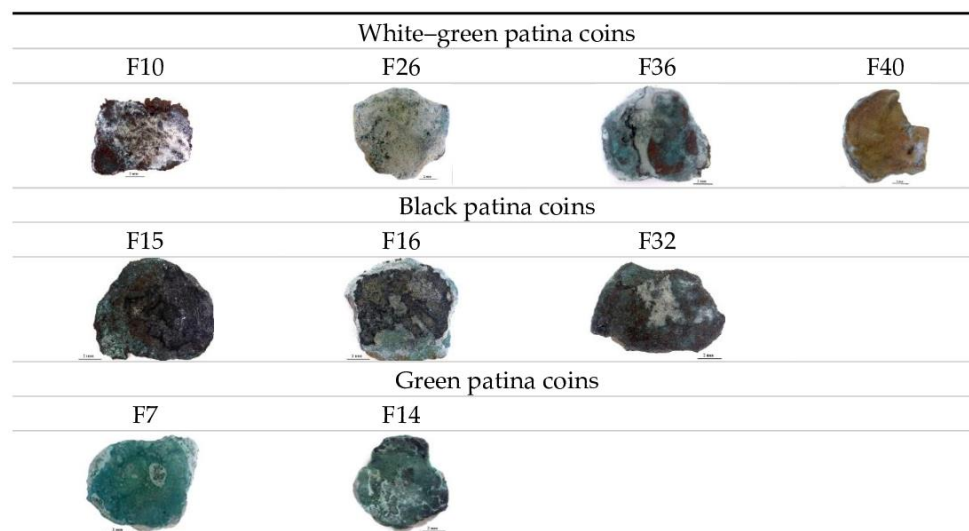


Figure 3. Antoninianus coins from Fontanamare wreck analyzed (photos: T. de Caro).

Table 1. Weight (g) and dimension (mm) of the analyzed coins.

	F10	F26	F36	F40	F15	F16	F32	F7	F14
Weight (g)	0.74	0.81	1.02	0.78	1.02	0.98	1.12	0.72	0.78
Dimension (mm)	10.6	10.8	11.6	9	13	12	15	11.2	11

2.2. Analytical Methods

The selected coins have been analyzed by means of optical microscopy (OM), scanning electron microscopy (SEM), energy-dispersive X-ray spectroscopy (EDS), X-ray diffraction (XRD) analysis, and micro-Raman (μ -Raman) spectroscopy.

Optical microscopy (OM) investigations were performed using a Leica M125 C microscope and a MEF 4 microscope equipped with a digital camera, Leica MC170 HD.

SEM and EDS characterizations were carried out by a LEO VP 1450 equipped with a microprobe X-ray INCA 300 and a four-sector backscattered electron detector (BSE). The beam accelerating voltage was set between 20 and 30 keV, sufficient to overcome the critical energy of the electrons for the X-ray emission (quantitative resolution limit of 0.2% by weight).

The structural identification of crystalline phases of the patinas was determined by a Siemens 5000 X-ray powder diffractometer using a Ni-filtered Cu K α radiation ($\lambda = 1.5418$). Angular values in the range between 10 and 80° in additive mode, a step size of 0.05°, and a sampling time of 2 s were the experimental parameters used for data acquisition. X-ray diffraction pattern analysis was carried out using RUFF online database [<https://ruff.info> accessed on 16 February 2023] and with the instrument library.

μ -Raman analysis was performed at room temperature using a Renishaw RM2000, equipped with a Peltier-cooled charge-coupled device (CCD) camera, in conjunction with a Leica optical microscope with $\times 10$, $\times 20$, $\times 50$, and $\times 100$ objectives. Measurements were performed using the $\times 50$ objective (laser spot diameter of about 1 μm) and the 514.5 nm excitation line of an Ar⁺ laser using the equipped density filter and with a real output of 300 μW . Raman analysis was carried out using RUFF online database [<https://ruff.info> accessed on 17 February 2023] with the GRAMS library.

3. Results

3.1. White–Green Patina Coins

The optical image of the F10 coin is shown in Figure 4A. To analyze the microchemical and microstructural features of the surface layer, SEM/EDS analyses (Figure 4B,D) were carried out. The SEM image shows a nonuniform patina, with light and dark areas of different chemical compositions observed through backscattered electrons, as evidenced by the EDS spectra recorded on the A, B, and C areas, where Pb, Sn, and Cu, and Cl and S elements are, respectively, present.

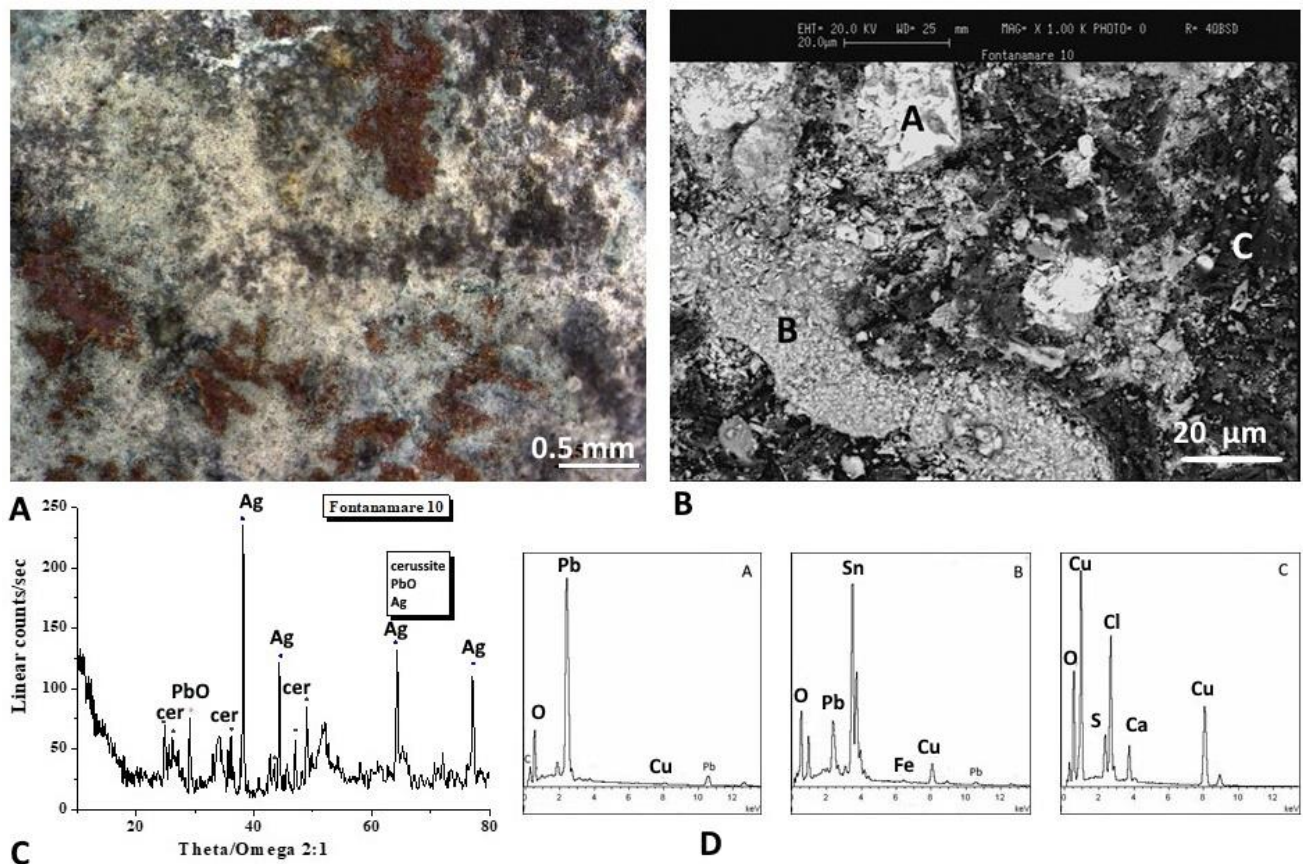


Figure 4. Surface analysis of coin F10: (A) Optical and (B) backscattered SEM images of coin surface. (C) XRD analysis that highlights the presence of the lead carbonate cerussite (PbCO₃) and the lead oxide. (D) EDS spectra recorded on the A, B, and C areas, where Pb, Sn, and Cu, and Cl and S elements are, respectively, present.

The nature of the corrosion products was identified by means of the XRD analysis (Figure 4C) and highlights the presence of Pb compounds such as the lead carbonates cerussite (PbCO_3) and the lead oxide.

The optical image of the F26 coin is shown in Figure 5A. The SEM image (Figure 5B) shows a nonuniform patina with a white area rich in Pb, Cl, and Sn and a dark area rich in Pb and Cl, as evidenced by the EDS spectra (Figure 5D).

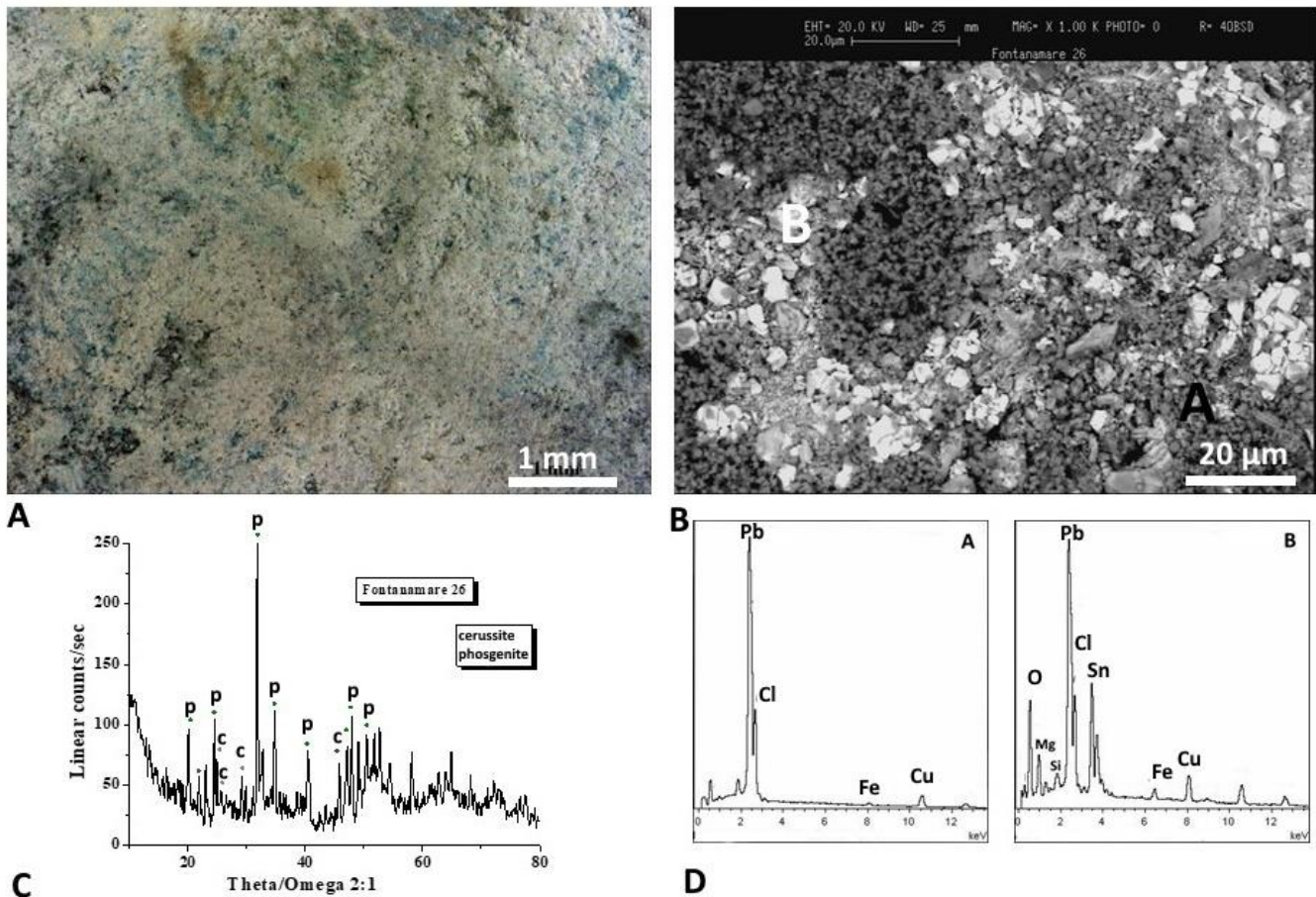


Figure 5. Surface analysis of coin F26. Characterizations of the artefacts: (A) optical and (B) backscattered images of coin surface. (C) XRD analysis that highlights the presence of cerussite and phosgenite (PbCl_2CO_3). (D) EDS spectra recorded on the A and B areas, where Pb, Cl, and Sn and a dark area rich in Pb and Cl elements are, respectively, present.

The XRD analysis (Figure 5C) defines the presence of cerussite as well as the lead chloro-carbonate phosgenite (PbCl_2CO_3).

Figure 6A shows the optical image of the F36 coin. The surface has a green and white patina that is primarily composed of Pb, Cu, and Cl, with darker layers composed of soil minerals as evidenced by EDS spectra (Figure 6B,D). The diffractogram (Figure 6C) reveals the presence of atacamite ($\text{Cu}_2\text{Cl}(\text{OH})_3$), botallackite ($\text{Cu}_2(\text{OH})_3\text{Cl}$), and cuprite (Cu_2O). These corrosion products are frequently found on bronze artefacts that have been buried in marine environments [22].

The optical image of the F40 coin is shown in Figure 7A. According to SEM and EDS spectra (Figure 7B,D), the brown–white patina is composed of Sn and Pb in the white region and Cu and Sn in addition to the soil components in the darker area. The diffractogram (Figure 6C) shows that cassiterite (SnO_2) and cuprite (Cu_2O) are the predominant component of the surface layer.

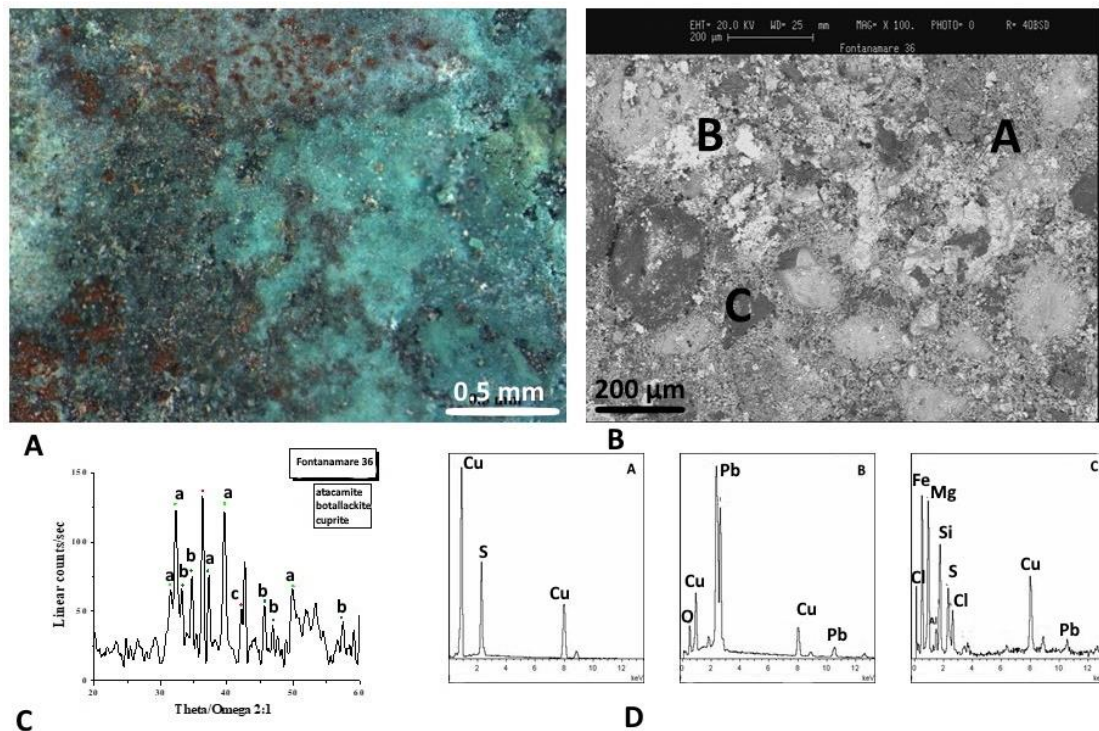


Figure 6. Surface analysis of coin F36. Characterizations of the artefacts: (A) optical and (B) backscattered SEM images of coin surface. (C) XRD analysis that highlights the presence of atacamite ($\text{Cu}_2\text{Cl}(\text{OH})_3$) (a), botallackite ($\text{Cu}_2(\text{OH})_3\text{Cl}$) (b), and cuprite (Cu_2O) (c). (D) EDS spectra recorded on the A, B, and C areas, where Pb, Cu, and Cl elements are, respectively, present.

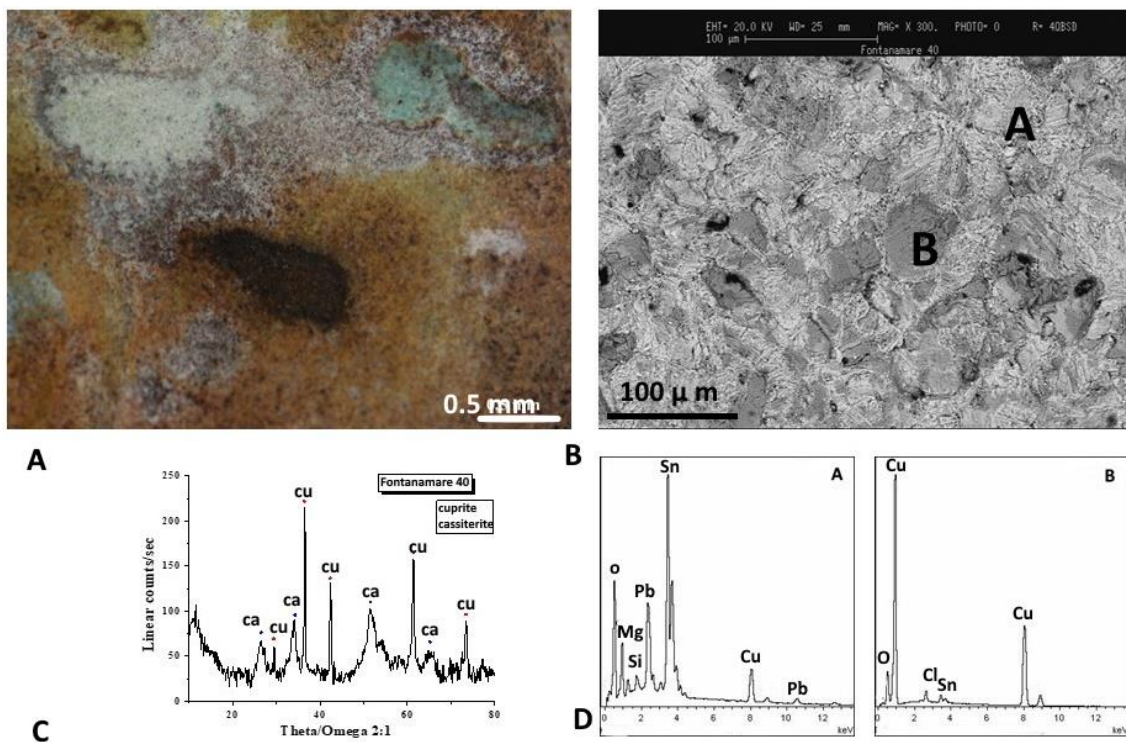


Figure 7. Surface analysis of coin F40. Characterizations of the artefacts: (A) optical and (B) backscattered SEM images of coin surface. (C) XRD analysis shows that cassiterite (SnO_2) and cuprite (Cu_2O) are the predominant component of the surface layer. (D) EDS spectra highlights the brown–white patina composed of Sn and Pb in the white region and Cu and Sn in addition to the soil components in the darker area.

3.2. Black Patina Coins

The optical image of the F15 coin is shown in Figure 8A. According to SEM and EDS spectra (Figure 8B,C), the patina is composed of Cu and S in the predominantly black areas.

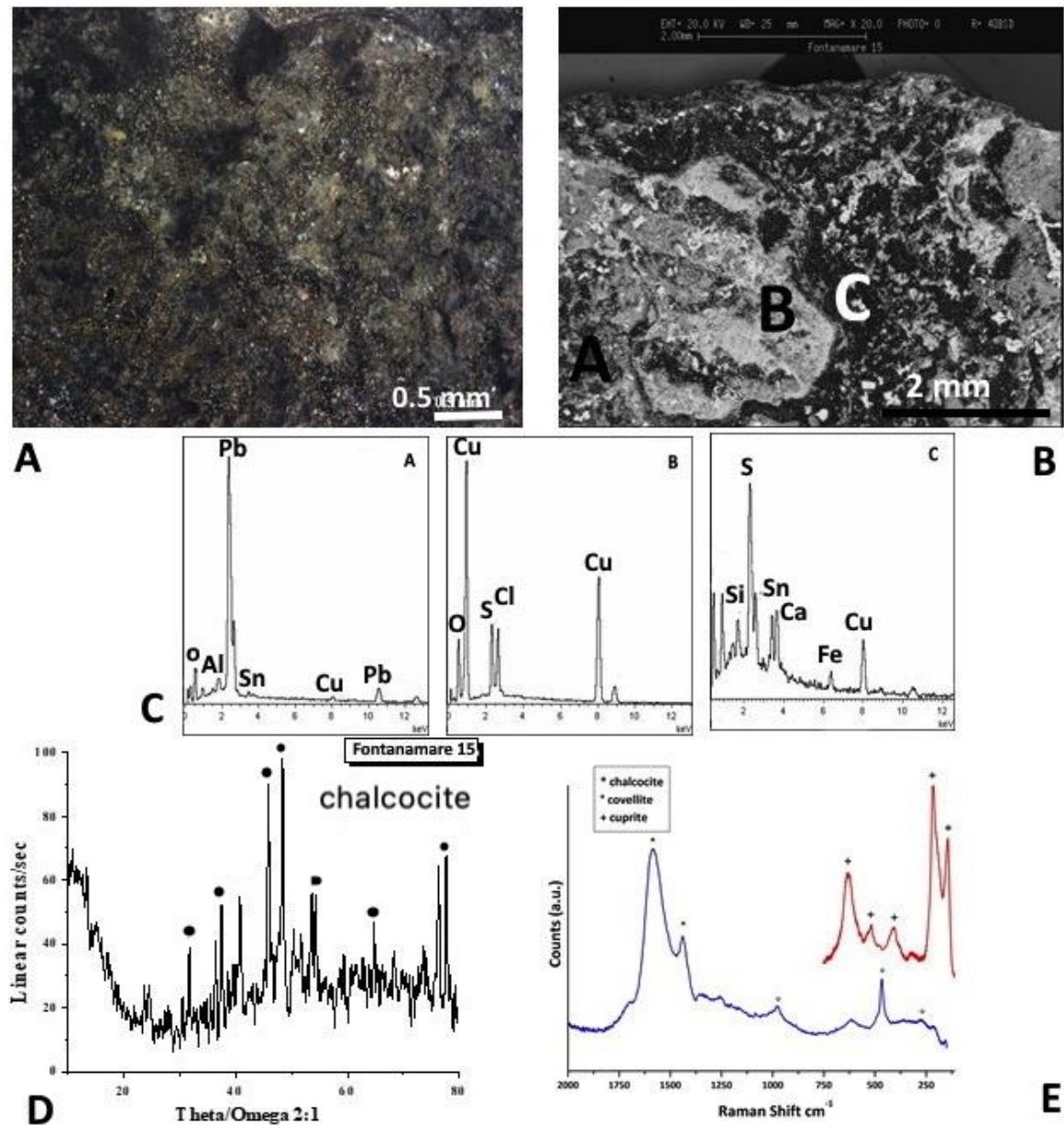


Figure 8. Surface analysis of coin F15. Characterizations of the artefacts: (A) optical and (B) backscattered SEM images of coin surface. (C) EDS spectra highlight that the patina is composed of Cu and S in the predominantly black areas. (D) XRD analysis evidences that Cu_2S (chalcocite) is formed as the primary component of the surface layer. (E) Raman spectra reveal the presence of CuS (covellite) and Cu_2S (chalcocite).

The nature of the corrosion products was defined by the XRD analysis and Raman spectra. The XRD pattern shown in Figure 8D provides further evidence that Cu_2S (chalcocite) formed as the primary component of the surface layer. The presence of additional copper sulphides, such as CuS (covellite), which form if the reactive sulphide anions are present, is revealed by the Raman spectrum of Figure 8E, obtained in a darker region.

The optical image of the F16 coin is shown in Figure 9A. According to the EDS spectra (Figure 9C), the patina is composed of Cu and S in the predominantly black areas.

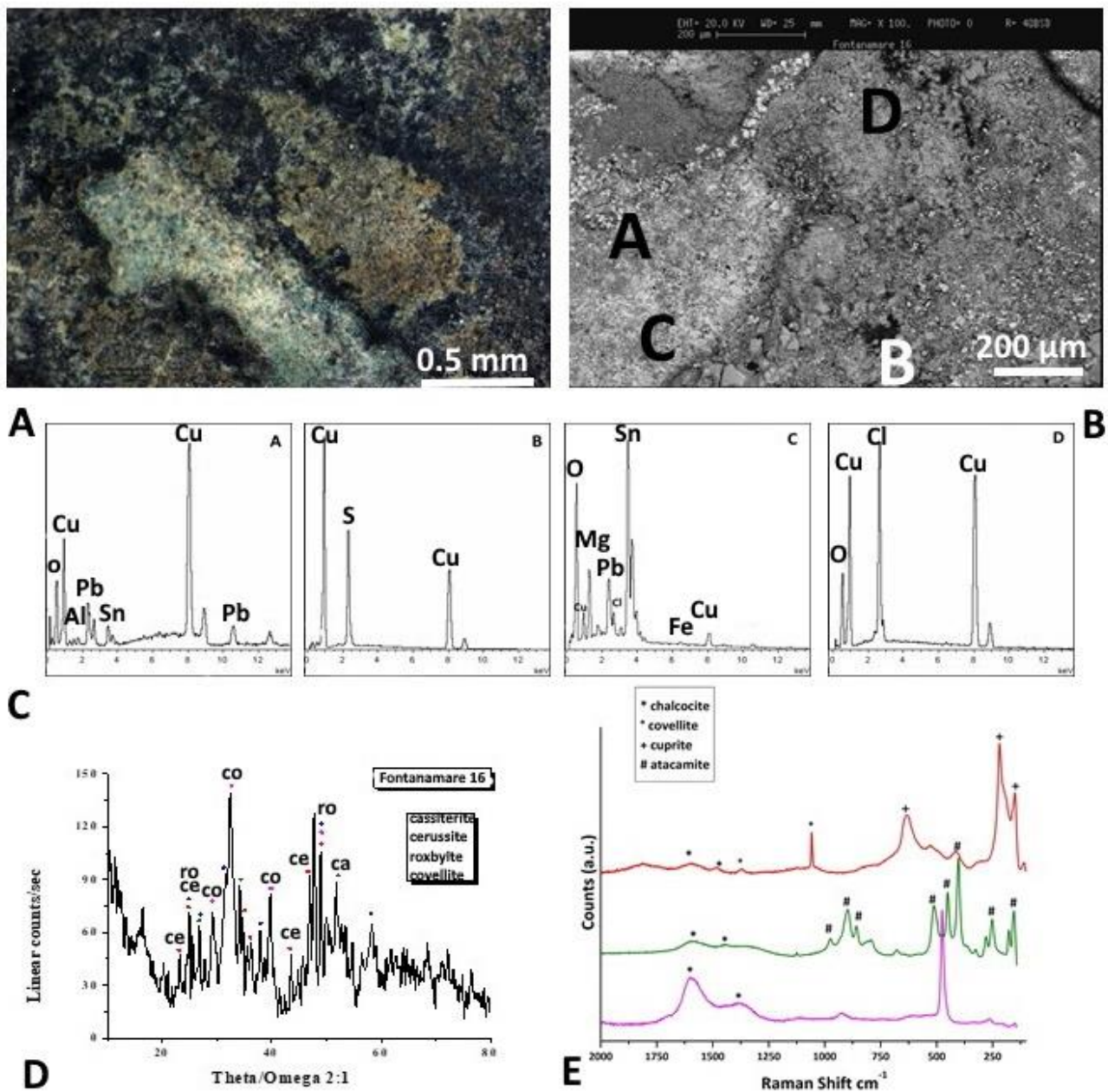


Figure 9. Surface analysis of coin F16. Characterizations of the artefacts: (A) optical and (B) backscattered SEM images of coin surface. (C) EDS spectra the patina is composed of Cu and S in the predominantly black areas and Sn and Pb in brighter area. (D) XRD analysis evidence that Cu_9S_5 (roxbylite), covellite (CuS), and chalcocite (Cu_2S) formed as the primary component of the surface layer of the dark zone and cassiterite (SnO_2) and cerussite (PbCO_3) as the primary component of the surface layer of the bright zone. (E) Raman spectrum reveals the presence of atacamite ($\text{Cu}_2\text{Cl}(\text{OH})_3$).

Several characterizations were performed to identify the microchemical and microstructural features of the surface layer, whose nonuniformity is evident in the SEM image of Figure 9B where brighter and darkened areas are present. The EDS spectra recorded on the A, B, C, and D areas, shown in Figure 9C, also reveal the presence of Sn and Pb in brighter area, and Cu, Cl, and S in darker areas.

The nature of the corrosion products was defined by the XRD analysis and Raman spectra. The XRD pattern and Raman spectra shown in Figure 9D,E provide further evidence that Cu_9S_5 (roxbyite), covellite (CuS), and chalcocite (Cu_2S) formed as the primary component of the surface layer of the dark zone and cassiterite (SnO_2) and cerussite (PbCO_3) as the primary component of the surface layer of the bright zone. The presence of atacamite ($\text{Cu}_2\text{Cl}(\text{OH})_3$) is revealed by the Raman spectrum of Figure 9E, obtained in a green region.

The optical image of the F32 coin is shown in Figure 10A. According to the EDS spectra (Figure 10D), the patina is composed of Cu and S in the predominantly black areas. The nature of the corrosion products is defined by the Raman spectra. The Raman spectra shown in Figure 10C provide evidence that covellite (CuS) and chalcocite (Cu_2S) united to cuprite (Cu_2O) formed as the primary component of the surface layer.

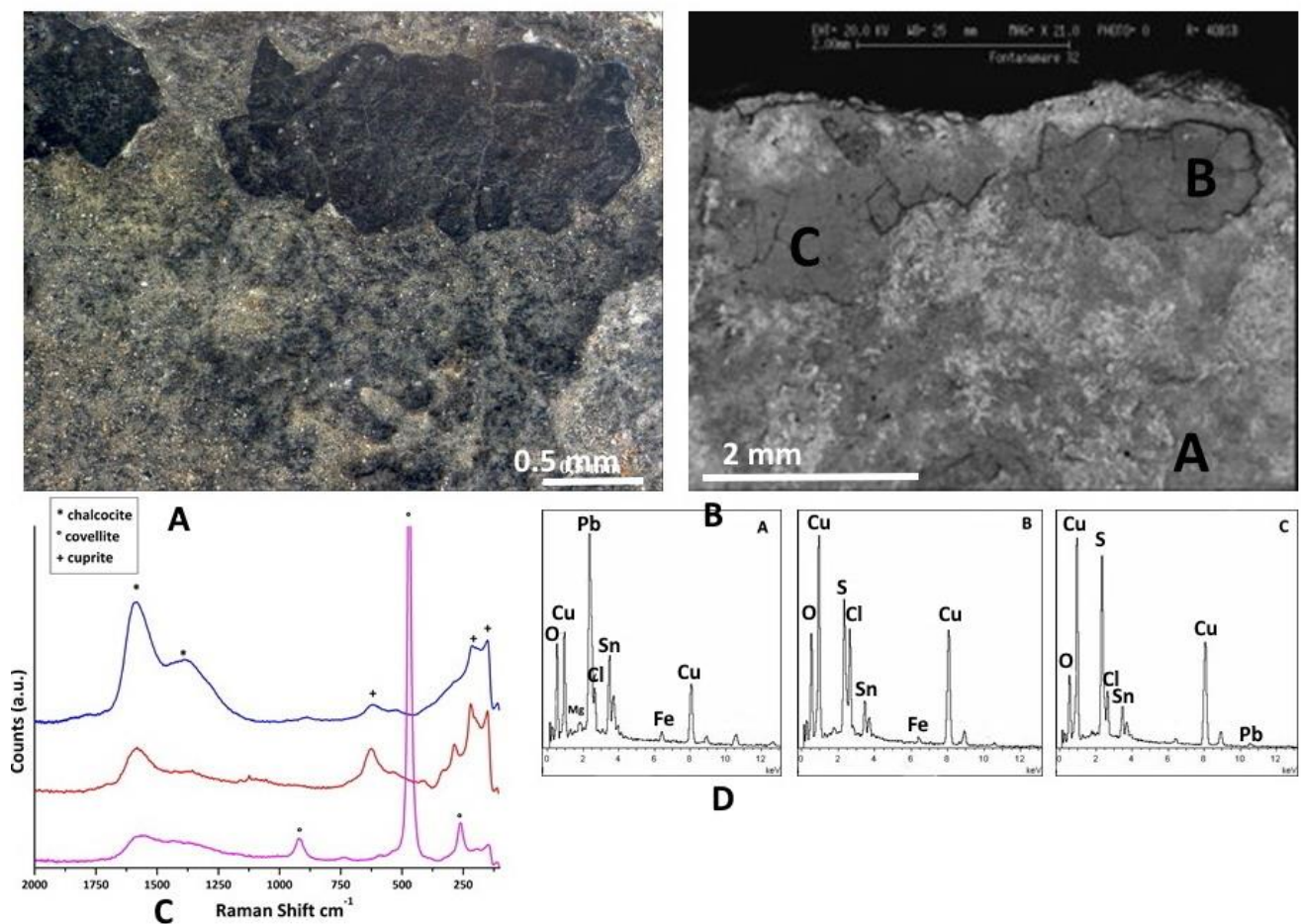


Figure 10. Surface analysis of coin F32. Characterizations of the artefacts: (A) optical and (B) back-scattered SEM images of coin surface. (C) Raman spectrum covellite (CuS) and chalcocite (Cu_2S) united to cuprite (Cu_2O) formed as the primary component of the surface layer. (D) EDS spectra the patina is composed Cu and S in the predominantly black areas.

The optical and SEM images of a metallographic section of F32 coin, shown in Figure 11A,B, evidence the morphological details of the patina of the artefact. The EDS spectra (Figure 10D) confirm a patina composed of copper sulphide, as confirmed by the Raman spectra (Figure 10C); white areas are composed principally of Pb, and grey areas are composed of Cu, Sn, Cl, and Fe. The optical image evidences that the bulk alloy is almost completely mineralized.

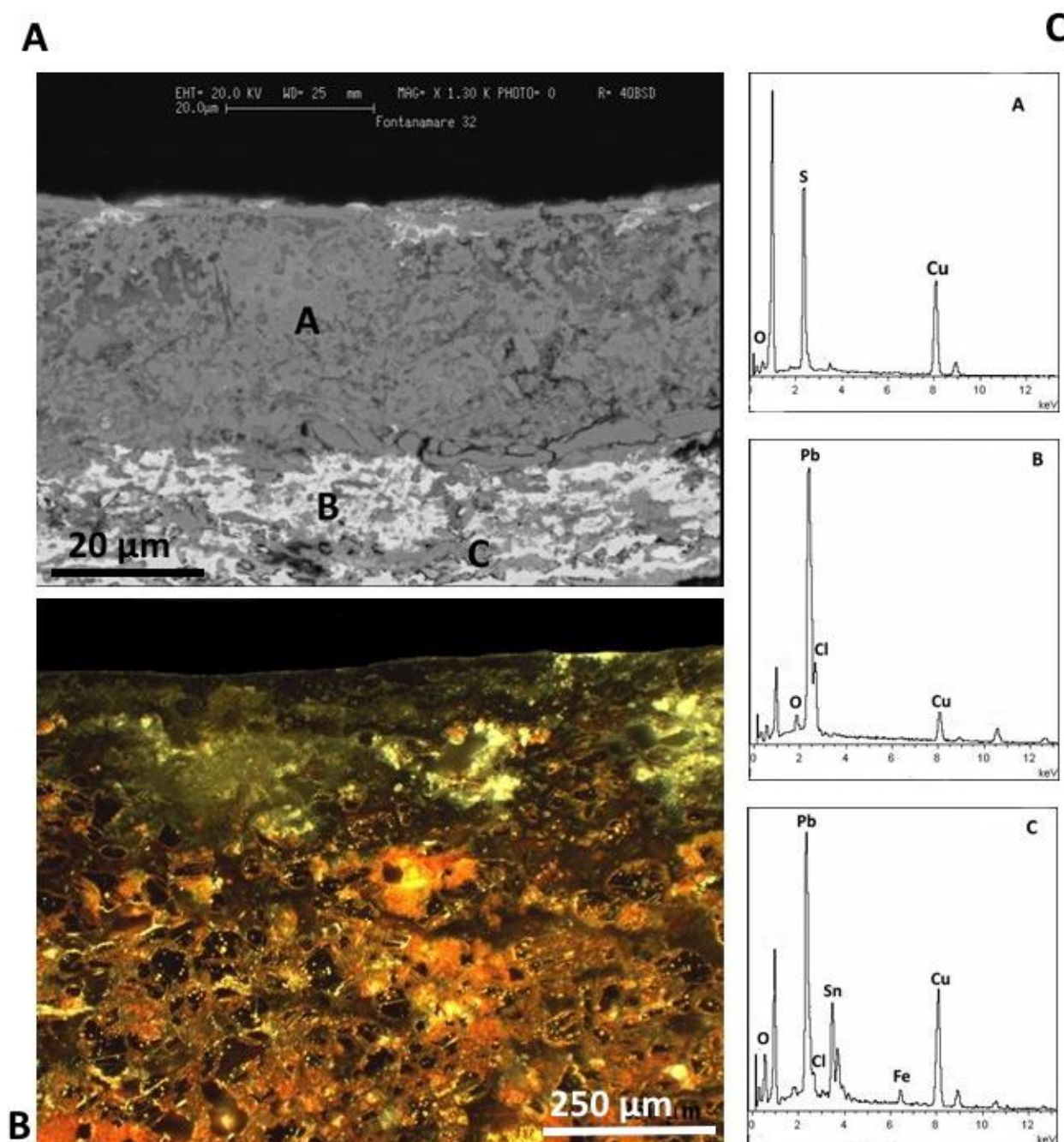


Figure 11. (A,B) SEM and optical images of a metallographic section of F32 coin. (C) EDS spectra confirm that the patina is composed of copper sulphide while white areas are composed principally of Pb, and grey areas are composed of Cu, Sn, Cl, and Fe. The optical image evidences that the coin is almost completely mineralized.

3.3. Green Patina Coins

The analytical results for the F7 and F14 coins are displayed in Figures 12–14. The surfaces have a stronger green patina that is predominantly made up of Pb, Cu, and Cl, as demonstrated by the EDS spectra in Figures 12 and 13B. Botallackite ($\text{Cu}_2(\text{OH})_3\text{Cl}$) and atacamite–clinoatacamite ($\text{Cu}_2\text{Cl}(\text{OH})_3$) are both present, according to the diffractograms. Moreover, the EDS spectrum of F14 coins (Figure 13D) reveals the presence of Ag on the coin's surface.

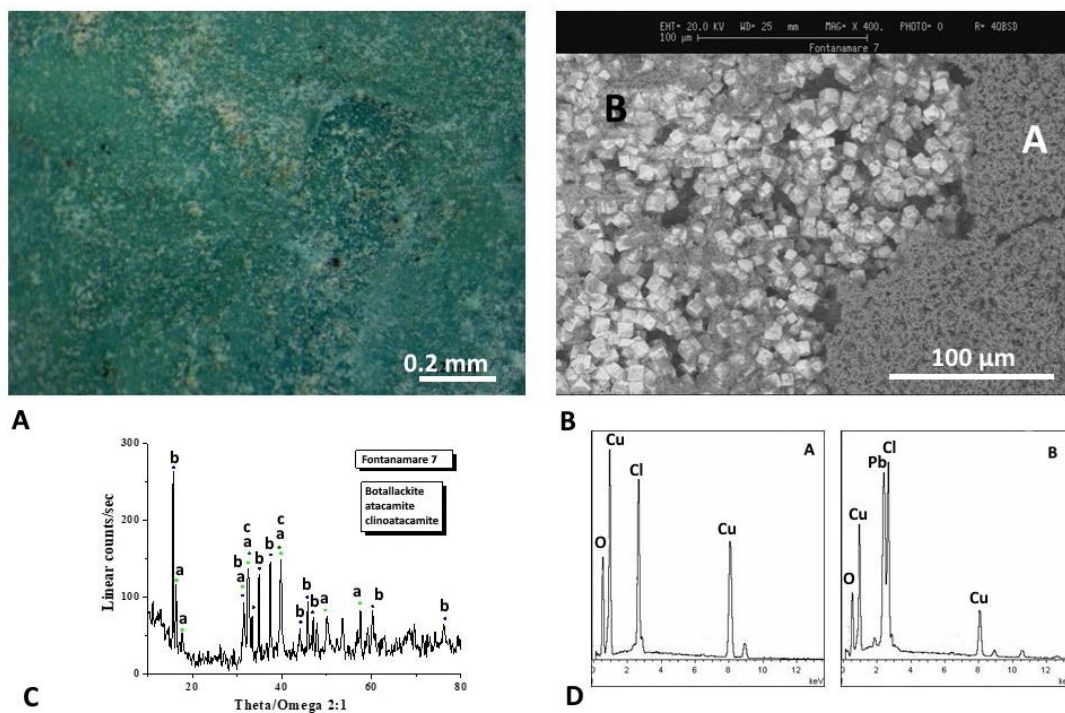


Figure 12. Surface analysis of coin F7. Characterizations of the artefacts: (A) optical images and (B) backscattered SEM images of coin surface. (C) XRD analysis shows that botallackite (b) ($\text{Cu}_2(\text{OH})_3\text{Cl}$) and atacamite–clinoatacamite (a,c) ($\text{Cu}_2\text{Cl}(\text{OH})_3$) are the predominant components of the surface layer. (D) EDS spectra highlights the presence of Pb, Cu, and Cl elements.

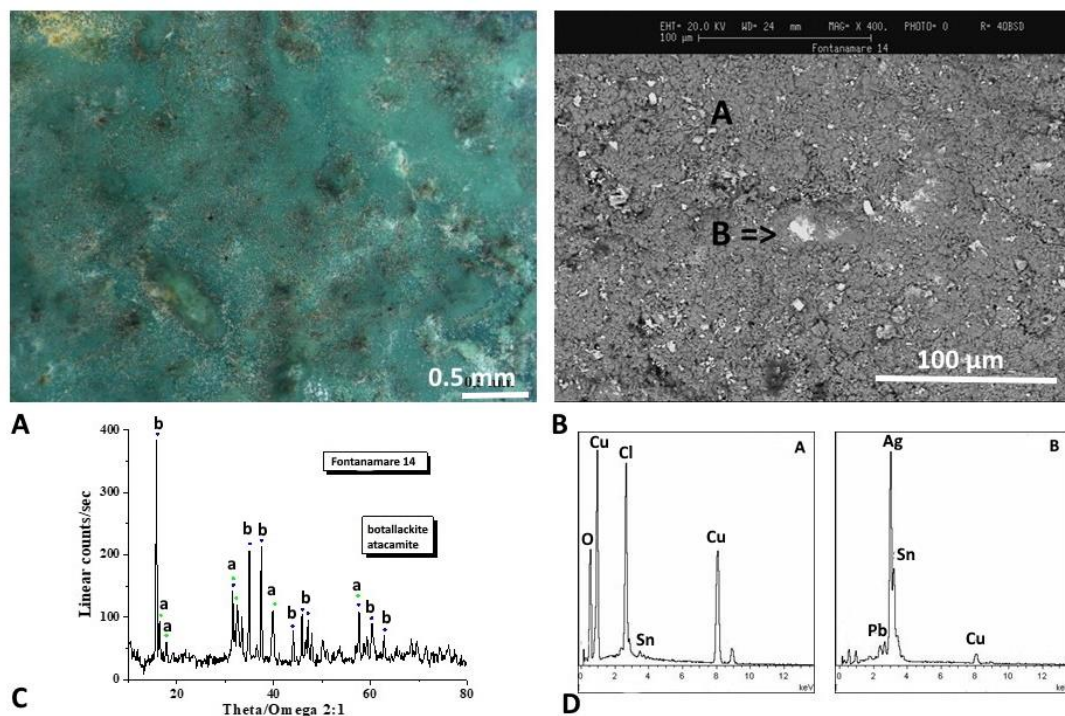


Figure 13. Surface analysis of coin F14. Characterizations of the artefacts: (A) optical images and (B) backscattered SEM images of coin surface. (C) XRD analysis shows that botallackite (b) ($\text{Cu}_2(\text{OH})_3\text{Cl}$) and atacamite–clinoatacamite (a,c) ($\text{Cu}_2\text{Cl}(\text{OH})_3$) are the predominant components of the surface layer. (D) EDS spectra highlights the presence of Pb, Cu, and Cl elements. Moreover, the EDS spectrum of F14 coins reveals the presence of Ag on the coin’s surface.

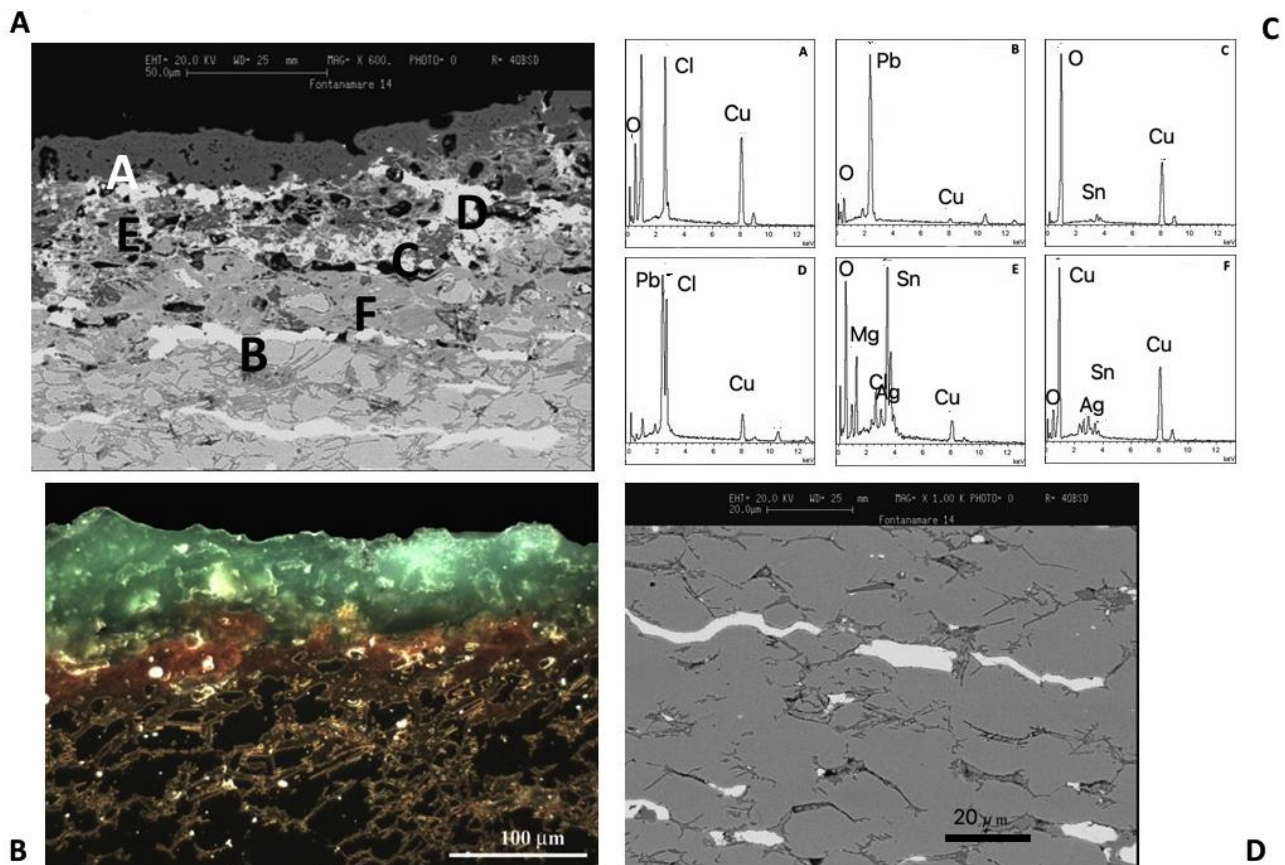


Figure 14. (A,B) SEM and optical images of a metallographic section of the F34 coin. (C) EDS spectra indicates that the external corrosion layer is composed of copper chloride hydroxide compounds. The optical image evidences that the coin is almost completely mineralized. (D) SEM image that evidence Pb phases with elongated morphology.

The optical and SEM images of a metallographic section of the F34 coin, shown in Figure 14A,B, evidence the morphological details of the patina of the artefact.

As was previously observed from the surface study shown in Figure 13, the EDS spectrum (Figure 13C, spectrum A) indicates that the external corrosion layer is composed of copper chloride hydroxide compounds [23].

4. Discussion

The analyses carried out on nine coins reveal a wide range of corrosion products related to the microchemistry and microstructure of the alloy, as well as the environment in which they were found.

The prevalent presence of white Pb compounds in F10 and F26 patinas is related to the alloy composition of the antoninianus coins, which hold high levels of Pb. Lead was frequently added to copper alloys to debase the coinage, since it was a less expensive metal than copper and tin in ancient times [24].

Lead-containing corrosion products, such as the cerussite shown in the XRD spectrum (Figure 4C), may be more prevalent in the patina as a result of lead segregating to the outer surface of the mould during casting. When the bronze contains isolated globules of lead, similar segregation events can take place, and, over time, Pb migrates to the alloy surface, where it reacts with ions from the environment to form Pb compounds [20]. Moreover, lead acetates and basic carbonates can form when leaded bronze items are in contact with wooden or fibre composites, glues, rubbers, and other materials, since lead is particularly susceptible to corrosion in the presence of organic acids [25]. The storage of Fontanamare

coins in a sack at the time of the shipwreck may have made it easier for Pb corrosion products to form.

The F10 patina XRD spectrum (Figure 4C) also evidences the presence of Ag, used as an alloying element in the manufacturing process of the antoninianus coins.

Phosgenite (PbCl_2CO_3), highlighted in the XRD spectrum of coin F26 (Figure 5C), may be related to the chlorine present in sea water.

The EDS results (Figures 4 and 5D) confirm the presence of Pb and Sn phases resulting from alloy composition and the presence of Cl resulting from the marine environment. The EDS spectrum of coin F10 (Figure 4C) highlights the presence of S, which probably originated from the decomposition of organic matter.

Copper chloride hydroxide (atacamite and botallackite) observed in the patina of coin F36 suggests a change in the hydroxyl/chloride ratio in the solution. Even though nantokite (CuCl) has not been found, it is likely that it acted as a precursor to the formation of atacamite, resulting in the cyclic oxidation and hydrolysis reactions known as bronze disease. This is the main corrosion process in a marine environment, and it is a very aggressive form of corrosion, which destroys the artefacts in a very short time, as in the case of the patina of the analyzed coins [25]. The cuprite phase, shown in XRD spectrum (Figure 6C), is stable at the pH range of seawater, which ranges between 6.2 and 9.2, according to the Pourbaix diagram for copper in oxygenated seawater at 25 °C, while the formation of cuprous chloride from cuprite is not favored [26]. Almost all saltwater has a pH that typically ranges around 8, but significant variations can occur in limited areas such as beneath concretions, and cuprous chloride can be observed in seawater as a corrosion product if the local pH level is low enough to promote its development [7].

The EDS results (Figure 6D) confirm the presence of Cl with Pb from the alloy, S from the decomposition of organic matter, and Fe and Mg sourced, most likely, from the burial site.

The patina of coin F40 shows a superficial Sn enrichment, as shown by the EDS spectrum (Figure 7D) that testifies to the decuprification phenomenon, which is the selective dissolution of the Cu, resulting in the surface of the alloy being enriched with Sn, which gives rise to cassiterite highlights in XRD spectrum (Figure 7C). In this case, the object is protected from corrosion by a passivation film formed when Sn oxidizes on the surface [27].

The F15, F16, and F32 coins show mainly black corrosion products composed of copper sulphides, as evidenced by XRD (Figures 8 and 9C) and Raman spectra (Figure 10C). In this case, sulphide ions are formed during burial conditions, where the reduction of sulphate ions by bacteria under anaerobic conditions can occur [28–32], and they can precipitate as copper sulphides with the copper ions coming from the artefacts. As the copper sulphides can range in color from greenish-black to blackish lead-grey to blue, the artefacts appearance can shift.

The process by which the copper sulphide is formed, as we have already mentioned, depends on a variety of factors, including the surface of the artefact, the sulphur content created by the decomposition of organic matter, and the nearly oxygen-free environment. The anaerobic conditions under the concretion created by biological colonization can stimulate microbial-induced corrosion (MIC), which would permit sulphate-reducing bacteria to grow due to sulphate-reducing bacteria (SRB) activity. Sulphate reduction is carried out by the SRB using sulphate as an electron acceptor. The oxidation of Cu combined with the reduction of sulphate is not thermodynamically favored. Therefore, free Cu^+ ions are transformed into copper sulphides such as chalcocite (Cu_2S), djurleite ($\text{Cu}_{1.97}\text{S}$), and covellite (CuS) by the S created during their growth [33].

The patina XRD and Raman spectra of coin F16 (Figure 9D,E), in addition to EDS spectra, point out the presence of Sn, Pb, and Cl in the form of cassiterite, cerussite, and atacamite, whose mechanisms of formation have already been described.

Coins F7 and F14 exhibit a patina made primarily of copper chloride hydroxide compounds that are green, emphasizing the aggressive type of bronze disease that can occur in marine conditions.

The EDS spectrum (Figure 13B) of coin F14 reveals the presence of Ag on the coin's surface, confirming the decuprification of the alloy, and a tin and silver enrichment on the external surface (Figure 13D spectrum B). As a result, tin and silver enrichment occurs on the external surface.

It should be noted that the content of Cu is low until 50 μm depth due to selective leaching. The alloy does not show visible corrosion at depths greater than 50 μm , below the boundary between the externally corroded layer and up to the inner core metal [34–36].

The metallographic section of F34 coin (Figure 14) evidences the microstructure of the alloy and confirms that they were made of a copper-based alloy with α -phase copper and lead phases lengthened along grain boundaries, which indicate the direction of the work hardening during the minting process [24].

The fact that lead has no solid solubility in copper and copper-based alloys should also be considered. When lead in a bronze alloy makes up more than a few percent of its weight, it appears as a dispersion of particles throughout the metal, and the number of these particles, known as globules, grows as the lead quantity increases [37–39].

Additionally, the cooling process of the alloy has a significant impact on the size and distribution of lead globules in the bronze artefacts. As a result, a leaded bronze object is not uniform at the microscale, and the corrosion products that arise have an extremely complicated microchemical structure. Slow cooling rates cause the formation of such lead globules in lead bronzes; indeed, if the alloy remains fluid for a long enough time, the lead, which does not form a solid-state solution, generates globules of significant dimension [24].

5. Conclusions

This study presents the first analysis of nine coins from a Roman shipwreck that occurred off the coast of Fontanamare, Sardinia. The coins have different patinas, demonstrating how small variations in the chemical and physical parameters can influence the nature of the patina. The first group of coins, characterized by a white/green patina, reveals the presence of predominantly Pb compounds, which could have been formed by the interaction of the alloy's Pb content with the natural fibers of the sack that held the coins at the time of the shipwreck. The second group reveals a primarily black patina, formed when bacteria reduce sulphate ions under anaerobic conditions. The final group of coins highlights the green patina and reveals the presence of copper chloride. The presence of chloride ions is thought to be dangerous because it triggers the copper cyclic corrosion reaction, which defaces the artefact and adversely affects its chemical–physical stability, as demonstrated in some case studies.

Finally, the metallographic section analysis confirms a heterogeneous copper–lead alloy with orientated α -copper grains and elongated lead phases, with low silver content, the result of the severe economic crisis preceding the time of the Constantine government.

Author Contributions: Conceptualization, T.d.C. and A.M.; validation, T.d.C., A.M., M.F.L.R. and F.S.; investigation, T.d.C. and A.M.; resources, T.d.C.; data curation, T.d.C. and A.M.; writing—original draft preparation, T.d.C.; writing—review and editing, A.M. and M.F.L.R.; visualization, A.M. and F.S.; supervision, T.d.C.; project administration, T.d.C. All authors have read and agreed to the published version of the manuscript.

Funding: This research received no external funding.

Institutional Review Board Statement: Not applicable.

Informed Consent Statement: Not applicable.

Data Availability Statement: Not applicable.

Acknowledgments: The authors acknowledge Claudio Veroli (ISMN-CNR) for skillful XRD technical assistance and Daniela Ferro for helpful SEM discussion.

Conflicts of Interest: The authors declare no conflict of interest.

References

1. Parker, A.J. Artifact Distributions and Wreck Locations: The Archaeology of Roman Commerce. *Mem. Am. Acad. Rome* **2008**, *6*, 177–196.
2. Pallarés, F. Fontanamare (Cagliari). Il relitto “A”. *Boll. Numis.* **2001**, 36–39, 9–151.
3. Faccenna, F. Fontanamare (Cagliari). Il relitto “A”. Il contesto monetale. *Boll. Numis.* **2001**, 36–39, 82–126.
4. Angelini, E.; Batmaz, A.; de Caro, T.; Faraldi, F.; Grassini, S.; Ingo, G.M.; Riccucci, C. The role of surface analysis in the strategies for conservation of metallic artefacts from the Mediterranean Basin. *Surf. Interface Anal.* **2014**, *46*, 754–763. [[CrossRef](#)]
5. Farro, N.W.; Veleva, L.; Aguilar, P. Copper Marine Corrosion: I. Corrosion Rates in Atmospheric and Seawater Environments of Peruvian Port. *Open Corros. J.* **2009**, *2*, 114–122. [[CrossRef](#)]
6. Veleva, L.; Farro, N.W. Influence of seawater on copper patina composition. *Appl. Surf. Sci.* **2012**, *258*, 10072–10076. [[CrossRef](#)]
7. Núñez, L.; Reguera, E.; Corvo, F.; González, E.; Vazquez, C. Corrosion of copper in seawater and its aerosols in a tropical island. *Corros. Sci.* **2005**, *47*, 461–484. [[CrossRef](#)]
8. Cohen, M.; Inberg, A.; Dana Ashkenazi, D.; Cvikel, D. What You Clean Is What You Get: A Novel Chemical Cleaning Technique and the Interpretation of Corrosion Products Found in Late Roman Copper Alloy Coins Retrieved from the Sea. *Heritage* **2022**, *5*, 3628–3647. [[CrossRef](#)]
9. Crisci, G.M.; La Russa, M.F.; Macchione, M.; Malagodi, M.; Palermo, A.M.; Ruffolo, S.A. Study of archaeological underwater finds: Deterioration and conservation. *Appl. Phys. A* **2010**, *100*, 855–863. [[CrossRef](#)]
10. Angelini, E.; Grassini, S.; Tusa, S. Underwater Corrosion of Metallic Heritage Artefacts. In *Corrosion and Conservation of Cultural Heritage Metallic Artefacts*; Woodhead Publishing: Sawston, UK, 2013; pp. 236–259. [[CrossRef](#)]
11. Macchia, A.; Colasanti, I.A.; Rivaroli, L.; Favero, G.; de Caro, T.; Munoz, L.P.; Campanella, L.; La Russa, M.F. Natural based products for cleaning copper and copper alloys artefacts. *Nat. Prod. Res.* **2023**, *37*, 1177–1184. [[CrossRef](#)]
12. MacLeod, I.D.; North, N.A. 350 years of marine corrosion in Western Australia. *Corros. Australas.* **1980**, *5*, 3.
13. Randazzo, L.; Ricca, M.; Pellegrino, D.; La Russa, D.; Marrone, A.; Macchia, A.; Rivaroli, L.; Enei, F.; La Russa, M.F. Anti-Fouling Additives for the Consolidation of Archaeological Mortars in Underwater Environment: Efficacy Tests Performed on the Apsidal Fishpond of Castrum Novum (Rome, Italy). *Int. J. Conserv. Sci.* **2020**, *11*, 243–250. Available online: <https://creativecommons.org/licenses/by-nc-nd/4.0/> (accessed on 7 March 2023).
14. Little, B.J.; Leeb, J.S.; Rayc, R.I. The influence of marine biofilms on corrosion: A concise review. *Electrochim. Acta* **2008**, *54*, 2–7. [[CrossRef](#)]
15. Bethencourt, M.; Tomás, F.-M.; Izquierdo, A.; González-Duarte, M.M.; Muñoz-Mas, C. a Study of the influence of physical, chemical and biological conditions that influence the deterioration and protection of Underwater Cultural Heritage. *Sci. Total Environ.* **2018**, *613*, 98–114. [[CrossRef](#)]
16. Elmouaden, K.; Jodeh, S.; Chaouay, A.; Oukhrib, R.; Salghi, R.; Bazzi, L.; Hilali, M. Sulfate-Reducing Bacteria Impact on Copper Corrosion Behavior in Natural Seawater Environment. *J. Surf. Eng. Mater. Adv. Technol.* **2016**, *6*, 36–46. [[CrossRef](#)]
17. Estalayo, E. Chemical study of degradation processes in ancient metallic materials rescued from underwater medium. *J. Raman Spectrosc.* **2019**, *50*, 289–298. [[CrossRef](#)]
18. Salvi, D. Mercanti e imperatori: Bolli, marchi e monete provenienti da scavi subacquei. In *Rivista Elettronica di Archeologia e Arte, Proceedings of Giornate di Studio di Archeologia e Storia dell'Arte a 20 Anni dall'Istituzione del Dipartimento di Scienze Archeologiche e Storico-Artistiche dell'Università degli Studi di Cagliari, Cagliari, Italy, 1–5 March 2010*; Dipartimento di Storia, Beni Culturali e Territorio dell'Università degli Studi di Cagliari Sezione di Archeologia e Storia dell'Arte Cittadella dei Musei: Cagliari, Italy, 2012.
19. Griesser, M.; Kockelmann, W.; Hradil, K.; Traum, R. New insights into the manufacturing technique and corrosion of high leaded antique bronze coins. *Microchem. J.* **2016**, *126*, 181–193. [[CrossRef](#)]
20. Craddock, P.T. The composition of the copper alloys used by the Greek, Etruscan and Roman civilizations. *J. Archaeol. Sci.* **1976**, *3*, 93–113. [[CrossRef](#)]
21. Pagano, S.; Balassone, G.; Germinario, C.; Grifa, C.; Izzo, F.; Mercurio, M.; Munzi, P.; Pappalardo, L.; Spagnoli, E.; Verde, M.; et al. Archaeometric Characterisation and Assessment of Conservation State of Coins: The Case-Study of a Selection of Antoniniani from the Hoard of Cumae (Campania Region, Southern Italy). *Heritage* **2023**, *6*, 2038–2055. [[CrossRef](#)]
22. North, N.; MacLeod, I. Corrosion of metals. In *Conservation of Marine Archaeological Objects*; Butterworth-Heinemann: Oxford, UK; Waltham, MA, USA, 1986; pp. 68–98. [[CrossRef](#)]
23. Scott, D.A. *Copper in Art—Copper and Bronze in Art: Corrosion, Colorants, Conservation*; Getty Publications: Los Angeles, CA, USA, 2002.
24. Inberg, A.; Ashkenazi, D.; Cohen, M.; Iddan, N.; Cvikel, D. Corrosion products and microstructure of copper alloy coins from the Byzantine-period Ma’agan Mikhael B shipwreck, Israel. *Microchem. J.* **2018**, *143*, 400–409. [[CrossRef](#)]
25. Scott, D.A. Bronze Disease: A review of some chemical problems and the role of relative humidity. *J. Am. Inst. Conserv.* **1990**, *29*, 193–206. [[CrossRef](#)]
26. Piccardo, P.; Mille, B.; Robbiola, L. Tin and copper oxides in corroded archaeological bronzes. In *Corrosion of Metallic Heritage Artefacts*; Woodhead Publishing: Sawston, UK, 2007; pp. 239–262. [[CrossRef](#)]
27. Robbiola, L.; Blengino, J.-M.; Fiaud, C. Morphology and mechanisms of formation of natural patinas on archaeological Cu–Sn Alloys. *Corros. Sc.* **1998**, *40*, 2083–2111. [[CrossRef](#)]
28. De Caro, T.; Caschera, D.; Ingo, G.M.; Calandra, P. Micro-Raman innovative methodology to identify Ag–Cu mixed sulphides as tarnishing corrosion products. *J. Raman Spectrosc.* **2016**, *47*, 852–859. [[CrossRef](#)]

29. Sánchez del Junco, A.; Moreno, D.A.; Ranninger, C.; Ortega-Calvo, J.J.; Sàiz-Jiménez, C. Microbial induced corrosion of metallic antiquities and works of art: A critical review. *Int. Biodeter. Biodegr.* **1992**, *29*, 367–375. [[CrossRef](#)]
30. MacLeod, M.B.; Jones, J.M.; Little, B.J. Production of sulfide minerals by sulfate reducing bacteria during microbiologically influenced corrosion of copper. *Corrosion* **1991**, *47*, 674–677.
31. Rémazeilles, C.; Langlet-Marzloff, V.; Creus, J.; Lotte, G.; Deshayes, C.; Baleux, F.; Robbiola, L. Remarkable corrosion resumption of archaeological bronzes, induced by the oxidation of ternary Cu-Sn-S phases in atmosphere, after long-term burial with sulfides. *Corros. Sci.* **2020**, *175*, 108865. [[CrossRef](#)]
32. Faraldi, F.; Cortese, B.; Caschera, D.; Di Carlo, G.; Riccucci, C.; de Caro, T.; Ingo, G.M. Smart conservation methodology for the preservation of copper-based objects against the hazardous corrosion. *Thin Solid Films* **2017**, *622*, 130–135. [[CrossRef](#)]
33. Armetta, F.; Ponterio, R.C.; Pibiri, I.; Saladino, M.L. New Insight on Archaeological Metal Finds, Nails and Lead Sheathings of the Punic Ship from Battle of the Egadi Islands. *Molecules* **2023**, *28*, 1968. [[CrossRef](#)]
34. Oudbashi, O.; Wanhill, R. Long-Term Embrittlement of Ancient Copper and Silver Alloys. *Heritage* **2021**, *4*, 2287–2319. [[CrossRef](#)]
35. Armetta, F.; Saladino, M.L.; Scherillo, A.; Caponetti, E. Microstructure and phase composition of bronze Montefortino helmets discovered Mediterranean seabed to explain an unusual corrosion. *Sci. Rep.* **2021**, *11*, 23022. [[CrossRef](#)] [[PubMed](#)]
36. Oudbashi, O.; Emami, S.M.; Ahmadi, H.; Davami, P. Micro-stratigraphical investigation on corrosion layers in ancient Bronze artefacts by scanning electron microscopy energy dispersive spectrometry and optical microscopy. *Herit. Sci.* **2013**, *1*, 21. [[CrossRef](#)]
37. Towarek, A.; Mistewicz, A.; Pilecka-Pietrusińska, E.; Zdunek, J.; Mizera, J. Corrosion degradation of archaeological lead: A review and case study. *J. Archaeol. Sci. Rep.* **2022**, *45*, 103611. [[CrossRef](#)]
38. Costa, V.; Urban, F. Lead and its alloys: Metallurgy, deterioration and conservation. *Conservation* **2005**, *6*, 48–62. [[CrossRef](#)]
39. Doménech-Carbó, M.T.; Di Turo, F.; Montoya, N.; Catalli, F.; Doménech-Carbó, A.; De Vito, C. FIB-FESEM and EMPA results on Antoninianus silver coins for manufacturing and corrosion processes. *Sci. Rep.* **2018**, *8*, 10676. [[CrossRef](#)] [[PubMed](#)]

Disclaimer/Publisher's Note: The statements, opinions and data contained in all publications are solely those of the individual author(s) and contributor(s) and not of MDPI and/or the editor(s). MDPI and/or the editor(s) disclaim responsibility for any injury to people or property resulting from any ideas, methods, instructions or products referred to in the content.